Networking and Positioning Co-Design in Multi-Connectivity Industrial mmW Systems

Elizaveta Rastorgueva-Foi, Olga Galinina, Mário Costa, *Member, IEEE,* Mike Koivisto, Jukka Talvitie, *Member, IEEE,* Sergey Andreev, *Senior Member, IEEE,* and Mikko Valkama, *Senior Member, IEEE*

***Abstract*—Highly directional millimeter-wave (mmW) connectivity – especially in industry-grade scenarios with complex and unpredictable device mobility – requires a certain degree of structural redundancy in the network, which can be provided by utilizing multi-connectivity mechanisms. To lower the coordination complexity and overhead of tracking multiple directional beams, mmW networks can retrieve and leverage timely positioning information. In this paper, we develop a holistic framework for the co-design of networking and positioning in industrial 5G mmW deployments with multi-connectivity capabilities. In particular, we propose a flexible two-stage positioning solution – mindful of information uncertainty – that relies upon the 5G NR system design and can be seamlessly integrated into the mmW cellular infrastructure with reasonable overheads. We reproduce a typical 5G mmW network deployment featuring dissimilar device mobility patterns and assess the performance of the proposed architecture. In particular, we evaluate the precision of our positioning and base station orientation estimation methods as well as analyze the impact of the proposed scheme on the system-level performance. Our numerical results demonstrate that the proposed solution yields highly accurate position estimates and significantly improves the average network spectral efficiency.**

***Index Terms*—5G New Radio, multi-connectivity, positioning and tracking, mobility, directionality, industrial verticals, mmW.**

I. Introduction

After the first full set of technical specifications for standalone 5G technology was frozen in September 2018, which is known as Release 15, 3rd Generation Partnership Project (3GPP) continued its work on the enhanced architecture options, such as 5G-5G dual-connectivity (see TS 37.340). As this initial 5G standard offers a stable foundation for early 5G deployments, the work is underway to facilitate 5G-and-beyond use cases for a diversity of vertical domains [1]. This includes support for cyber-physical control applications (see TS 22.104) and maritime services (see TS 22.119) over 3GPP systems.

Both maritime and cyber-physical communications are examples of Industrial Internet scenarios [2] and, as such, have many specific requirements, which are very different from those in other verticals or for the legacy systems. These are primarily along the lines of high reliability and low end-to-end latency demands when sharing real-time information between connected machines at various steps of a production cycle [3] or in other industrial facilities. In this context, the reliance of 5G new radio (NR) operation on a more abundant millimeter wave (mmW) spectrum allows it to potentially outperform even the best of today's real-time Ethernet networks [4].

The prospective industrial mmW deployments need to tame the unique features of radio connectivity in this band: primarily, vulnerability to link blockage by potentially moving obstacles and the need for extreme directionality to combat severe propagation losses. Fortunately, breakthroughs were made in the understanding of highly directional and blockage-aware mmW connectivity at both physical (PHY) [5]–[7] and medium access control (MAC) [8]–[11] layers. It was made clear that robust short-range networking requires certain types of structural redundancy, e.g., *multi-connectivity* [12], which is a form of macrodiversity that extends the conventional notion of dual-connectivity by enabling a device to maintain simultaneous links with two or more mmW base stations (BSs) [13].

The utilization of multi-connectivity mechanisms that facilitate the efficient operation of highly-directional 5G mmW networks may lead to substantial signaling overheads when tracking multiple directional beams. However, in the light of heavy reliance of mmW communications on the line-of-sight (LoS) links, reusing the network radio resources could ensure higher levels of positioning accuracy [14]–[18] without incurring a significant overhead, thus, simplifying the coordination complexity. Fortunately, flexible 5G NR numerology creates a room for incorporating network-based positioning functionality, and 3GPP has already summarized some of the envisioned use cases and their requirements for Release 16 (see TR 22.872).

Location-based beamforming seamlessly incorporated into the existing architecture will considerably reduce the levels of overhead and latency, thus, enabling more efficient multi-connectivity operation and boosting the network performance in general. Alongside mmW beamforming procedures, accurate positioning information might also be utilized by the higher network layers to facilitate more efficient load-balancing, radio resource management, and handover procedures [19]–[21].

The literature coverage of dynamic positioning for 5G mmW cellular networks remains limited, with substantial efforts in the vehicular context [15], [17] and further contributions on

This work was supported by the Academy of Finland under the projects 328214 ULTRA, 319994 FUWIRI, 317533 CROWN, 326196 RADIANT, and 323244 LOCALCOM; by Business Finland under the projects 5G-FORCE and 5G-VIIMA, and by the RAAS Connectivity RTF Framework.

E. Rastorgueva-Foi, O. Galinina, M. Koivisto, J. Talvitie, S. Andreev, and M. Valkama are with Tampere University, Tampere, Finland. Contact e-mail: elizaveta.rastorgueva-foi@tuni.fi

M. Costa is with Huawei Technologies Oy (Finland) Co Ltd

This article contains additional multimedia material.

joint user positioning and orientation estimation [22]. Recent fundamental positioning-related results in [23], [24], also applicable to mmW networks, target the localization accuracy in the cases where either the network is optimized for the positioning applications or the positioning algorithm is tailored to the network geometry. This emphasizes the need for a holistic framework that facilitates the *co-design of reliable networking and accurate positioning* in industrial mmW deployments with multi-connectivity capabilities, which we aim to develop in this paper.

In particular, the contributions of this work are as follows:

- We construct a scalable two-stage architecture for device positioning that can be integrated into an industrial mmW network deployment with multi-connectivity capabilities.
- We propose a novel positioning solution for tracking of the device locations and estimation of the orientation uncertainty at the BSs using downlink (DL) reference signal received power (RSRP) measurements. The proposed method extends our approach in [25] by incorporating power-based direction of departure (DoD) information, which enables joint 3D orientation estimation and positioning.
- Relying on a representative evaluation scenario with a typical 5G cellular deployment (e.g., an automated maritime container terminal depicted in Fig. 1 [26]–[28]), we demonstrate that our proposed framework is capable of achieving high accuracy of positioning and orientation estimation under complex device mobility patterns.
- We thoroughly evaluate the impact of an uncompensated BS orientation uncertainty and positioning inaccuracy on the network performance. The accompanying analysis demonstrates that while our system outperforms the conventional beamforming methods in terms of the average network spectral efficiency, incorporating the orientation uncertainty information results in further performance improvements.

The rest of this article is organized as follows. Section II introduces the main system modeling assumptions. The proposed two-stage positioning solution is detailed in Section III, while Section IV outlines the evaluation scenario. Finally, Section V provides the results of our numerical study, and Section VI concludes the paper. Selected further details of the tracking solution are provided in the Appendix.

II. System Model and Assumptions

In this section, we outline the system model and core assumptions of the proposed framework with respect to the deployment scenario. We further introduce the employed BS orientation uncertainty model and describe the beam-based RSRP measurement estimation procedure. The main system parameters are summarized in Table I.

A. Network Deployment and Antenna Properties

We study a 5G mmW network that covers a rectangular area of interest and comprises L stationary BSs, the exact 3D locations of which are known to the system. Within the target area, we consider K dynamic users (termed user equipments, UEs) with multi-connectivity capabilities, which implies that for each UE, there exist LoS links to several BSs at the same time. The UE motion follows certain mobility patterns (see Section IV-B for details); their initial locations are random and are distributed uniformly within the area.

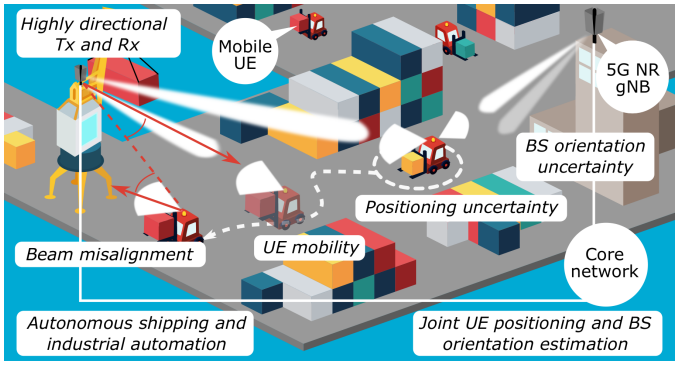

Fig. 1: Example industrial mmW deployment in an automated maritime container terminal.

Both BSs and UEs are assumed to be equipped with highly directional mmW antenna arrays having $\mathcal{M}_{\mathrm{BS}}$ and $\mathcal{M}_{\mathrm{UE}}$ beams, respectively. The positioning algorithm does not impose any further constraints on the BS and UE arrays; however, to ensure the existence of the LoS channel to several BS simultaneously, the UE array should have a relatively wide coverage. In particular, we assume that UEs rely on 2D beamforming and, thus, control their antenna radiation patterns in the azimuth plane covering 360°. The BSs can steer the antenna beams in both azimuth and elevation planes. The directivity gain of a single UE/BS antenna is denoted as $G_{\mathrm{UE/BS}}(\Delta\varphi, \Delta\vartheta)$, where $\Delta\varphi$ and $\Delta\vartheta$ are the azimuth and the co-elevation angles between the boresight of the antenna array and the direction at which the power is measured, further referred to as antenna misalignment.

The information on the BS orientations is available with a certain level of accuracy. In our model, we explicitly consider non-zero bearing and downtilt angle differences between the actual orientation of the BS antenna array and its orientation as assumed by the network. This 3D BS orientation uncertainty can be described by the azimuth and elevation uncertainty angles denoted as ϕ and θ, respectively. The BS orientation uncertainty is assumed to be relatively small (i.e., $|\theta|, |\phi| \leq 5°$) and time-invariant during the considered time frame. The uncompensated orientation information used in location-based beamforming should be estimated by the mmW network accurately. Otherwise, it may lead to significant positioning errors and cause severe channel gain degradation in the case of highly directional transmissions.

B. Transmission and Reception of Reference Signals

We assume that each BS periodically transmits beamformed orthogonal frequency-division multiplexing (OFDM)-based reference signals (RSs) regardless of the connection state of the UEs within the service area. In a 5G NR system, RSs can be represented by, for instance, a set of synchronization signal (SS)-blocks (see TS 38.211). The time interval between the

TABLE I: SUMMARY OF MAIN SYSTEM PARAMETERS AND QUANTITIES

Notation	Description
L, K	Number of BSs and UEs
$\mathcal{M}_{\mathrm{BS}}$ / $\mathcal{M}_{\mathrm{UE}}$	Number of BS / UE beams
ϑ, φ	Co-elevation and azimuth angles
θ, ϕ	BS orientation uncertainty (co-elevation, azimuth)
G_{UE} / G_{BS}	Gain of UE / BS antenna
τ	Time interval between two consecutive RS emissions
$\mathcal{M}_f$	Number of subcarriers
b_{UE} / b_{BS}	Complex-valued UE / BS antenna pattern
$\boldsymbol{n}$	Measurement noise
$\tilde{\sigma}^2$	Measurement noise variance
P_{tx} / P_{rx}	Transmit / receive power
$\boldsymbol{y}$	OFDM RS observation at the UE
$\boldsymbol{S}$	Transmitted OFDM symbol
$\boldsymbol{b}_f$	Channel frequency response
γ	Channel path weight
β	BRSRP measurement

two consecutive transmissions of RS used for positioning is denoted as τ. Note that τ can be equal to one or more DL RS emission periods for a specific beam. For example, in the case of SSs, τ corresponds to the SS burst set period.

The RSs are then received by the UE as per the receiver (Rx) beam sweeping process, which is illustrated in Fig. 2. The BS beams are assumed to be orthogonal, thus ensuring that the UE is able to distinguish different BS beams. This assumption typically holds in mmW systems, where either the BS beams are orthogonal in terms of the reference symbol sequences, or beamformed RSs are transmitted for different beams in a time-multiplexed manner.

For the LoS propagation, the multicarrier DL RS observation $\boldsymbol{y}_{i,j} \in \mathbb{C}^{\mathcal{M}_f}$ at the UE is given by

$$\boldsymbol{y}_{i,j} = \boldsymbol{S}\boldsymbol{b}_f b^i_{\mathrm{UE}}(\vartheta_a, \varphi_a) b^j_{\mathrm{BS}}(\vartheta_d, \varphi_d)\gamma_{i,j} + \boldsymbol{n}_{i,j}, \qquad (1)$$

where the subscripts i and j refer to the ith UE Rx beam and the jth BS transmitter (Tx) beam, respectively. Furthermore, $\boldsymbol{S} \in \mathbb{C}^{\mathcal{M}_f \times \mathcal{M}_f}$ is a diagonal matrix representing the transmitted frequency-domain reference symbols, while $\boldsymbol{b}_f \in \mathbb{C}^{\mathcal{M}_f}$ is the frequency response of the channel and Tx-Rx radio frequency chains, and $\mathcal{M}_f$ denotes the number of subcarriers. The complex-valued beam pattern of the jth BS beam is denoted as $b^j_{\mathrm{BS}}(\vartheta_d, \varphi_d) \in \mathbb{C}$, while $b^i_{\mathrm{UE}}(\vartheta_a, \varphi_a) \in \mathbb{C}$ addresses the corresponding beam pattern of the ith UE beam.

Here, the departure co-elevation and azimuth angles at the BS are referred to as (ϑ_d, φ_d), while (ϑ_a, φ_a) stands for the corresponding arrival co-elevation and azimuth angles at the UE side. Finally, the complex-valued path weight between the considered beam pair is denoted as $\gamma_{i,j} \in \mathbb{C}$, and the measurement noise is accounted for as $\boldsymbol{n}_{i,j}$. We assume that the latter is a complex circular Gaussian random variable distributed with the zero mean: $\boldsymbol{n}_{i,j} \sim \mathcal{N}_C(\boldsymbol{0}, \tilde{\sigma}^2\boldsymbol{I}) \in \mathbb{C}^{\mathcal{M}_f}$, and it is uncorrelated and independent of the beam pair, i.e., $\tilde{\sigma}^2_{i,j} = \tilde{\sigma}^2, \forall i, j$, where $\tilde{\sigma} \in \mathbb{R}$ is unknown.

Further, we define the beam reference signal received power (BRSRP) measurement $\beta_{i,j}$ for the ith UE Rx beam and the jth BS Tx beam. In particular, according to 3GPP TS 38.215, $\beta_{i,j} \in \mathbb{R}$ – as measured and quantized by the UE – relates to the multicarrier observation given in (1) as follows:

$$\beta_{i,j} = \frac{1}{\mathcal{M}_f}\sum_{k=1}^{\mathcal{M}_f} |[\boldsymbol{y}_{i,j}]_k|^2, \qquad (2)$$

where $i = 1, \ldots, \mathcal{M}_{\mathrm{UE}}$, $j = 1, \ldots, \mathcal{M}_{\mathrm{BS}}$, and $\mathcal{M}_{\mathrm{UE/BS}}$ denotes the number of beams at the UE/BS.

In our assumptions, reporting the BRSRP measurements back to the BS does not require any specific feedback channel. The only condition is that the DL RS transmission and reception as well as the feedback transmission and reception occur within the time interval of τ. Since the proposed positioning algorithm is essentially angle-based, it does not impose further restrictions on the time synchronization within the network or between UEs and BSs other than those necessary for the communication purposes. Typically, synchronization within the cyclic prefix (CP) length is required, which is at the microsecond level, unlike the nanosecond-level synchronization needed for the time-based positioning [29], [30]. In addition, our approach does not demand any range measurements. We also emphasize that the proposed solution exploits the existing spatial multiplexing features and does not rely upon the actual structure of the utilized RSs. Therefore, it is assumed that any periodic beamformed DL RS may be employed.

III. POSITIONING ARCHITECTURE AND METHOD

In this section, we introduce a novel solution that offers not only accurate 3D UE positioning but also provides estimation and tracking of possible BS orientation uncertainties. The uncompensated inaccuracy of orientation information may lead to significant positioning errors and cause severe channel gain degradation in highly directional systems with location-based beamforming. Hence, the BS orientation uncertainty should also be estimated accurately by the network. In what follows, we outline the two-stage positioning architecture and detail the proposed estimation algorithms. The general structure of our positioning scheme is summarized in Algorithm 1, while the main algorithmic notations are summarized in Table II.

A. Two-Stage Positioning Architecture

The proposed positioning procedure is based upon the BRSRP measurements converted into the DoD angle estimates. The obtained angle estimates are then utilized in the subsequent joint UE positioning and BS orientation uncertainty estimation. Our proposed approach is naturally decomposed into two stages, which are schematically illustrated in Fig. 2 and described in Algorithm 1. Particularly, BSs transmit beamformed RSs that are received by all of the connected UEs directionally. At the first stage of the proposed positioning procedure, the BRSRPs measured at the UEs are reported back to the corresponding BS, where the BRSRP measurements are then converted into the DoD angle estimates using extended Kalman filter (EKF)-based solutions.

At the second stage, these DoD angle estimates from all of the BSs are collected by the network and fused into the UE location and the BS orientation uncertainty estimates by employing a novel EKF-based approach. This two-stage

Algorithm 1 Two-stage EKF for joint 3D UE positioning and BS orientation uncertainty estimation

for every time-instant $n = 0, 1, 2, \ldots, N$

  for every available BS in the network

    step 1: The BS transmits beamformed DL reference signals using all Tx beams.

    step 2: Each UE measures the BRSRPs for all Tx-Rx beam pairs with the BSs.

    step 3: Each UE selects the Rx beam corresponding to the largest sum of BRSRP measurements over all Tx beams.

    step 4: According to the selected Rx beam, each UE reports $\mathcal{M}_{\text{BS}}$ BRSRP measurements and Tx beams in a feedback channel.

    step 5: Based on the received BRSRP measurements, the BS estimates and tracks the DoD of each UE using the EKF. After that, the obtained DoD estimates of all UEs are delivered to the central network control unit.

  end for

  step 6: 3D UE positions and BS orientation uncertainties are estimated jointly and tracked in the network by collecting the DoD estimates from all BSs in the second EKF-based solution.

end for

architecture allows the network to distribute the computations associated with each stage, thus, decreasing the computational burden of the users. Another advantage of the proposed two-stage architecture is a possibility to use the DoD angle estimates derived at the first stage of the EKF, directly for the BS beamforming in DL. Alongside the direct DL beamforming, the UE positioning information obtained at the second stage can be further utilized by the enhanced location-based beamforming on the newly established connection, e.g., in the case of a reconnection after a LoS-blockage or in a handover procedure.

We employ the EKFs in both first – the DoD angle estimation – and second – the UE positioning and BS orientation estimation – phases. The EKF, as a sequential estimator, utilizes the information on the state evolution as well as the previous measurements, by remaining computationally more attractive than the commonly used numerical solutions, such as particle filters. Due to the use of such prior information, sequential estimation methods allow for assessing and tracking larger state vectors even in the cases of smaller numbers of observations.

We adopt and devise the so-called information form of the EKF, which is less computationally complex as compared to the conventional Kalman-gain form, especially when the state vector has smaller dimensions than the observation vector. For example, in the case of the available beam-based measurements for $\mathcal{M}_{\text{BS}} = 64$ beams and the state vector of two variables (ϑ, φ) in the first-stage EKF, only a 2×2 matrix needs to be inverted in the information form of the EKF. For the corresponding Kalman-gain version of the EKF, inversion of a 64×64 matrix is required. In the following, we first address

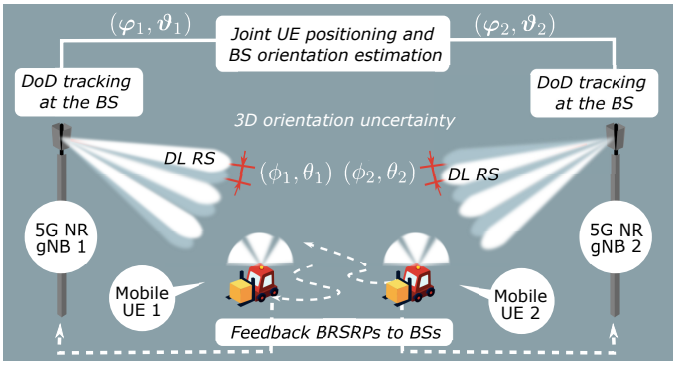

Fig. 2: Illustration of proposed architecture. Each BS (with a small orientation misalignment) directionally transmits DL-RSs. Based on received DL-RSs, each active UE first measures BRSRPs for each BS and then delivers quantized BRSRPs to the corresponding BSs in a feedback channel. The BRSRP measurements are used for estimating and tracking the DoDs at the BSs to facilitate joint positioning, orientation uncertainty estimation, and user tracking at the central network node.

the first-stage DoD estimation and tracking EKFs that utilize BRSRP measurements at each BS. Then, we formulate the proposed second-stage EKF, which subsequently fuses the DoD estimates from the first-stage EKFs into the joint 3D UE location and BS orientation uncertainty estimates.

B. Stage 1: Proposed EKF for RS-Based DoD Tracking

Let us denote the vector of BRSRP measurements at a given time instant n as $\boldsymbol{\beta}[n] = [\beta_{i^*,1}[n], \ldots, \beta_{i^*,\mathcal{M}_{\text{BS}}}[n]]^{\text{T}} \in \mathbb{R}^{\mathcal{M}_{\text{BS}}}$, where $i^* = \arg\max_i \sum_{j=1}^{\mathcal{M}_{BS}} \beta_{i,j}[n]$ stands for the index of the Rx beam with the largest sum of the measured BRSRP values over all of the BS beams. Note that the particular method of selecting the receiving UE beam index i^* is not essential for the operation of our algorithm.

More specifically, the measurement vector $\boldsymbol{\beta}[n]$ is determined in the process of beam search and is reported back to the BS through the appropriate feedback procedures. In addition, let us denote the state vector of the DoD estimation and tracking EKF at the time instant n as $\boldsymbol{s}_{DoD}[n] \in \mathbb{R}^4$. In particular, $\boldsymbol{s}_{DoD}[n] = [\vartheta[n], \varphi[n], \dot{\vartheta}[n], \dot{\varphi}[n]]^{\text{T}}$, where $\vartheta[n] \in [0, \pi]$ and $\varphi[n] \in [0, 2\pi)$ are the co-elevation and azimuth departure angles from the BS to the UE, while $\dot{\vartheta}[n]$ and $\dot{\varphi}[n]$ are the corresponding rates of change.

We assume that the state of the considered system evolves according to a continuous white-noise acceleration (CWNA) model; hence, the prediction step of the EKF is given in a linear form as in [31]:

$$\begin{aligned} \boldsymbol{s}^{-}_{DoD}[n] &= \boldsymbol{F}_{DoD}\boldsymbol{s}^{+}_{DoD}[n-1] \\ \boldsymbol{C}^{-}_{DoD}[n] &= \boldsymbol{F}_{DoD}\boldsymbol{C}^{+}_{DoD}[n-1]\boldsymbol{F}^{\text{T}}_{DoD} + \boldsymbol{Q}_{DoD}, \end{aligned} \tag{3}$$

where $\boldsymbol{F}_{DoD} \in \mathbb{R}^{4\times4}$ is the state-transition matrix, $\boldsymbol{Q}_{DoD} \in \mathbb{R}^{4\times4}$ is the process noise covariance matrix, and $\boldsymbol{C}^{-}_{DoD} \in \mathbb{R}^{4\times4}$ is the *a priori* covariance matrix of the state. After the prediction step of the EKF, the available BRSRP measurements are incorporated into the estimation process as part of the update

TABLE II: SUMMARY OF MAIN EKF NOTATIONS

Notation	Description
$\boldsymbol{p}$	3D position of the UE
$\dot{x}$	Rate of change of x
Δx	Difference / distance in x
$\boldsymbol{s}^{-}_{DoD/pos}$	State prediction, DoD-tracking / positioning EKF
$\boldsymbol{s}^{+}_{DoD/pos}$	State update, ————————————"————
$\boldsymbol{F}_{DoD/pos}$	State-transition matrix, ————————"————
$\boldsymbol{C}^{-}_{DoD/pos}$	Covariance matrix prediction, ————-"————
$\boldsymbol{C}^{+}_{DoD/pos}$	Covariance matrix update, ————————"————
$\boldsymbol{Q}_{DoD/pos}$	State-noise covariance matrix, ————-"————
$\boldsymbol{\mathcal{I}}$	Observed Fisher information matrix
$\boldsymbol{q}$	Gradient of log-likelihood function
$\tilde{\vartheta}, \tilde{\varphi}$	Co-elevation and azimuth DoD angles corrupted by BS orientation uncertainty
$\boldsymbol{\varepsilon}$	Vector of estimated DoD angles
$\boldsymbol{\xi}$	Mean of $\boldsymbol{\varepsilon}$

step of the EKF [31]

$$\begin{aligned} \boldsymbol{C}^{+}_{DoD}[n] &= \left(\boldsymbol{C}^{-}_{DoD}[n]^{-1} + \boldsymbol{\mathcal{I}}(\boldsymbol{s}^{-}_{DoD}[n])\right)^{-1} \\ \Delta\boldsymbol{s}_{DoD}[n] &= \boldsymbol{C}^{+}_{DoD}[n]\, \boldsymbol{q}(\boldsymbol{s}^{-}_{DoD}[n]) \\ \boldsymbol{s}^{+}_{DoD}[n] &= \boldsymbol{s}^{-}_{DoD}[n] + \Delta\boldsymbol{s}_{DoD}[n], \end{aligned} \tag{4}$$

where $\boldsymbol{\mathcal{I}}(\boldsymbol{s}^{-}[n]) \in \mathbb{R}^{4\times 4}$ denotes the observed Fisher information matrix (FIM) and $\boldsymbol{q}(\boldsymbol{s}^{-}_{DoD}[n]) \in \mathbb{R}^{4}$ is the gradient of the log-likelihood function of the state given the BRSRP measurements $\boldsymbol{\beta}[n]$. Further details of the first-stage EKF derivations are provided in the Appendix for the reader's convenience. Importantly, to estimate and track the DoD angles, the DoD-EKF relies upon the directions of the Tx beams.

C. Stage 2: Proposed EKF for Joint UE Positioning and BS Orientation Uncertainty Tracking

In the proposed second-stage EKF, the azimuth and co-elevation DoD angle estimates from the first-stage DoD-EKFs are fused into the 3D location estimates of the UEs and the orientation uncertainty estimates of the available BSs in a sequential manner. Let us denote the 3D location of the kth UE in the global Cartesian coordinate system as $\boldsymbol{p}_k = [x_k, y_k, z_k]^{\mathrm{T}} \in \mathbb{R}^3$, where $k = 1, \ldots, K$, K is the number of active UEs. The actual DoD angles of the LoS path between the kth UE and the ℓth BS at a time instant n are $(\vartheta^{\ell}_{k}[n], \varphi^{\ell}_{k}[n])$, where $\ell = 1, \ldots, L$.

We also introduce a pair of variables $(\tilde{\vartheta}^{\ell}_{k}[n], \tilde{\varphi}^{\ell}_{k}[n])$, which are network-assumed DoD angles distorted by the orientation uncertainties, i.e.,

$$\begin{aligned} \tilde{\vartheta}^{\ell}_{k}[n] &= \vartheta^{\ell}_{k}[n] + \theta_{\ell}, \\ \tilde{\varphi}^{\ell}_{k}[n] &= \varphi^{\ell}_{k}[n] + \phi_{\ell} \mod 2\pi \\ & \qquad k = 1, \ldots, K, \quad \ell = 1, \ldots, L, \end{aligned} \tag{5}$$

where $\theta_{\ell} \in [0, \pi]$ and $\phi_{\ell} \in [0, 2\pi)$ stand for the orientation uncertainty of the ℓth BSs in the elevation and the azimuth directions, respectively.

Let us consider vectors $\tilde{\boldsymbol{\vartheta}}[n] \in \mathbb{R}^{KL}$ and $\tilde{\boldsymbol{\varphi}}[n] \in \mathbb{R}^{KL}$ that contain distorted co-elevation and azimuth angles between K UEs and L BSs as given in (5)

$$\begin{aligned} \tilde{\boldsymbol{\vartheta}}[n] &= [\tilde{\vartheta}^{1}_{1}[n], \ldots, \tilde{\vartheta}^{L}_{1}[n], \tilde{\vartheta}^{1}_{2}[n], \ldots, \tilde{\vartheta}^{L}_{K}[n]]^{\mathrm{T}} \\ \tilde{\boldsymbol{\varphi}}[n] &= [\tilde{\varphi}^{1}_{1}[n], \ldots, \tilde{\varphi}^{L}_{1}[n], \tilde{\varphi}^{1}_{2}[n], \ldots, \tilde{\varphi}^{L}_{K}[n]]^{\mathrm{T}}. \end{aligned} \tag{6}$$

The corresponding DoD estimates obtained from the first-stage DoD-EKFs are denoted as $\hat{\boldsymbol{\vartheta}}[n] \in \mathbb{R}^{KL}$ and $\hat{\boldsymbol{\varphi}}[n] \in \mathbb{R}^{KL}$ for the co-elevation and the azimuth directions, respectively, and

$$\begin{bmatrix} \hat{\boldsymbol{\vartheta}}[n] \\ \hat{\boldsymbol{\varphi}}[n] \end{bmatrix} \sim \mathcal{N}\left(\begin{bmatrix} \tilde{\boldsymbol{\vartheta}}[n] \\ \tilde{\boldsymbol{\varphi}}[n] \end{bmatrix}, \boldsymbol{C}[n] \right), \tag{7}$$

where $\tilde{\boldsymbol{\vartheta}}[n]$ and $\tilde{\boldsymbol{\varphi}}[n]$ are the DoD angles affected by the BS orientation uncertainties (6).

Finally, the covariance matrix for the DoD estimates $\boldsymbol{C}_{DoD}[n] \in \mathbb{R}^{2KL\times 2KL}$ is given by

$$\boldsymbol{C}_{DoD}[n] = \text{blkdiag}\left\{\boldsymbol{C}^{1}_{1}[n], \ldots, \boldsymbol{C}^{L}_{1}[n], \boldsymbol{C}^{1}_{2}[n], \ldots, \boldsymbol{C}^{L}_{K}[n]\right\}, \tag{8}$$

where blkdiag$\{\cdot\}$ represents a block-diagonal matrix. In (8), each $\boldsymbol{C}^{\ell}_{k}[n] \in \mathbb{R}^{2\times 2}$ equals to the upper-left (2×2) sub-matrix of the *a posteriori* covariance matrix $\boldsymbol{C}^{+}_{DoD}[n]$ in the DoD-EKF (see Section III-B). For the sake of simplicity, we assume that $\boldsymbol{C}_{DoD}[n]$ is independent of $\tilde{\boldsymbol{\vartheta}}[n]$ and $\tilde{\boldsymbol{\varphi}}[n]$.

For the proposed second-stage EKF, we denote the state vector as $\boldsymbol{s}_{pos} \in \mathbb{R}^{6K+4L}$:

$$\boldsymbol{s}_{pos} = [\boldsymbol{p}^{\mathrm{T}}_{1}, \ldots, \boldsymbol{p}^{\mathrm{T}}_{K}, \boldsymbol{\theta}^{\mathrm{T}}, \boldsymbol{\phi}^{\mathrm{T}}]^{\mathrm{T}}, \tag{9}$$

where $\boldsymbol{p}_k$ is the 3D location of the kth UE, while $\boldsymbol{\theta} \in \mathbb{R}^{L}$ and $\boldsymbol{\phi} \in \mathbb{R}^{L}$ are the orientation uncertainties of L BSs in the elevation and the azimuth domain, respectively.

According to the continuous white-noise velocity (CWNV) state propagation model, the prediction step of the EKF is given as

$$\begin{aligned} \boldsymbol{s}^{-}_{pos}[n] &= \boldsymbol{F}_{pos}\boldsymbol{s}^{+}_{pos}[n-1] \\ \boldsymbol{C}^{-}_{pos}[n] &= \boldsymbol{F}_{pos}\boldsymbol{C}^{+}_{pos}[n-1]\boldsymbol{F}^{\mathrm{T}}_{pos} + \boldsymbol{Q}_{pos}, \end{aligned} \tag{10}$$

where $\boldsymbol{F}_{pos} \in \mathbb{R}^{(6K+4L)\times(6K+4L)}$ is the linear state-transition matrix, $\boldsymbol{C}_{pos} \in \mathbb{R}^{(6K+4L)\times(6K+4L)}$ is the state-covariance matrix, and $\boldsymbol{Q}_{pos} \in \mathbb{R}^{(6K+4L)\times(6K+4L)}$ is the state-noise covariance matrix.

We employ CWNV model for the state dynamics of both the UE location and the BS orientation uncertainties. Hence, the matrices $\boldsymbol{F}_{pos}$ and $\boldsymbol{Q}_{pos}$ can be established, e.g., as per [32, Ch.2]. The update step equations of the second-stage EKF are given here in a general form:

$$\begin{aligned} \boldsymbol{C}^{+}_{pos}[n] &= \left(\boldsymbol{C}^{-}_{pos}[n]^{-1} + \boldsymbol{\mathcal{I}}_{\boldsymbol{pos}}(\boldsymbol{s}^{-}_{pos}[n])\right)^{-1} \\ \Delta\boldsymbol{s}_{pos}[n] &= \boldsymbol{C}^{+}_{pos}[n]\, \boldsymbol{q}(\boldsymbol{s}^{-}_{pos}[n]) \\ \boldsymbol{s}^{+}_{pos}[n] &= \boldsymbol{s}^{-}_{pos}[n] + \Delta\boldsymbol{s}_{pos}[n], \end{aligned} \tag{11}$$

where $\boldsymbol{\mathcal{I}}(\boldsymbol{s}^{-}_{pos}[n]) \in \mathbb{R}^{(6K+4L)\times(6K+4L)}$ denotes the observed FIM, while $\boldsymbol{q}(\boldsymbol{s}^{-}_{pos}[n]) \in \mathbb{R}^{(6K+4L)}$ represents the gradient of the log-likelihood function of the UE positions and the BS orientation uncertainty given the DoD estimates from multiple BSs.

To derive the observed FIM $\mathcal{I}(\boldsymbol{s}_{pos}^{-}[n])$ and the gradient of the log-likelihood function $\boldsymbol{q}(\boldsymbol{s}_{pos}^{-}[n])$, we denote the estimated DoDs of L BSs toward K UEs as $\boldsymbol{\varepsilon} = [\hat{\boldsymbol{\vartheta}}^{\mathrm{T}}, \hat{\boldsymbol{\varphi}}^{\mathrm{T}}]^{\mathrm{T}} \in \mathbb{R}^{2KL}$. From (7), it follows that $\boldsymbol{\varepsilon} \sim \mathcal{N}(\boldsymbol{\xi}(\boldsymbol{s}_{pos}), \boldsymbol{C}_{\boldsymbol{\varepsilon}})$, where

$$\begin{aligned} \boldsymbol{\xi}(\boldsymbol{s}_{pos}) &= \left[\tilde{\boldsymbol{\vartheta}}^{\mathrm{T}}(\boldsymbol{s}_{pos}), \tilde{\boldsymbol{\varphi}}^{\mathrm{T}}(\boldsymbol{s}_{pos})\right]^{\mathrm{T}} \\ \boldsymbol{C}_{\boldsymbol{\varepsilon}} &= \mathrm{blkdiag}\left\{\boldsymbol{C}_1^1, \ldots, \boldsymbol{C}_1^L, \boldsymbol{C}_2^1, \ldots, \boldsymbol{C}_K^L\right\}. \end{aligned} \tag{12}$$

One may rewrite the DoD angles in (5) as a function of $\boldsymbol{s}_{pos}$ as

$$\begin{aligned} \tilde{\vartheta}_k^{\ell}(\boldsymbol{s}_{pos}) &= \arctan 2\left(d_{2\mathrm{D}_k^{\ell}}, \Delta z_k^{\ell}\right) + \theta_{\ell}, \\ \tilde{\varphi}_k^{\ell}(\boldsymbol{s}_{pos}) &= \arctan 2\left(\Delta y_k^{\ell}, \Delta x_k^{\ell}\right) + \phi_{\ell}, \end{aligned} \tag{13}$$

where $d_{2\mathrm{D}_k^{\ell}} = \sqrt{{\Delta x_k^{\ell}}^2 + {\Delta y_k^{\ell}}^2}$, while $\Delta x_k^{\ell} = x_{\mathrm{UE}_k} - x_{\mathrm{BS}_{\ell}}$, $\Delta y_k^{\ell} = y_{\mathrm{UE}_k} - y_{\mathrm{BS}_{\ell}}$, and $\Delta z_k^{\ell} = z_{\mathrm{UE}_k} - z_{\mathrm{BS}_{\ell}}$ are the distances between the kth UE and the ℓth BS along the axes of the global coordinate system. The expressions for the gradient of the log-likelihood function of $\boldsymbol{s}_{pos}$ and for the respective observed FIM follow from [33, Ch.3] as:

$$\begin{aligned} [\boldsymbol{q}(\boldsymbol{s}_{pos})]_m &= \left(\frac{\partial \boldsymbol{\xi}(\boldsymbol{s}_{pos})}{\partial [\boldsymbol{s}_{pos}]_m}\right)^{\mathrm{T}} \boldsymbol{C}_{\boldsymbol{\varepsilon}}^{-1}\left(\boldsymbol{\varepsilon} - \boldsymbol{\xi}(\boldsymbol{s}_{pos})\right), \\ [\mathcal{I}(\boldsymbol{s}_{pos})]_{m,n} &\approx \left(\frac{\partial \boldsymbol{\xi}(\boldsymbol{s}_{pos})}{\partial [\boldsymbol{s}_{pos}]_m}\right)^{\mathrm{T}} \boldsymbol{C}_{\boldsymbol{\varepsilon}}^{-1} \frac{\partial \boldsymbol{\xi}(\boldsymbol{s}_{pos})}{\partial [\boldsymbol{s}_{pos}]_n}. \end{aligned} \tag{14}$$

IV. Evaluation Scenario and Settings

In this section, we outline the target industrial application scenario, which is followed for the subsequent evaluation of the proposed framework and methods. As a concrete example, we consider an automated container port deployment setup that was depicted in Fig. 1.

A. Deployment Scenario and Mobility

In today's world of highly intensive trade and shipping services, an automated maritime container terminal, termed "smart port" or "smart harbor", is one of the popularly envisioned deployment scenarios for 5G-and-beyond networks [26]–[28]. For example, 5G port automation was deployed and is currently being tested in multiple container terminals around the world [35]–[38]. In terms of the radio channel modeling, we follow METIS methodology [34] on a Madrid grid, which we adjust to represent a container terminal (see Fig. 3) with the stockpiles of metal containers and concrete storage buildings. The parameters of the deployed mmW system are presented in Table III.

In our setup, BSs represent 5G NR gNBs, and UEs correspond to automated guided vehicles (AGVs), which are semi-autonomous container-hauling vehicles. The AGVs are expected to function autonomously with a possibility for a remote operator to intervene in case of emergency; hence, their mobility pattern depends on the type of routing. For example, the simplest fixed-path routing allows AGVs to travel along pre-programmed trajectories, which can be captured by a deterministic routing model. More complex routing models include dynamic routing wherein AGVs move in a mesh layout. Further, free-range routing, which allows AGVs to use the entire available area for motion and independent decision-making, can be implemented in the system of collaborative AGVs with distributed control methods. More complex routing improves the performance of the transport system at the expense of increased signaling and computational loads [39]–[41].

In the subsequent numerical evaluation, we model two extreme cases of the AGV routing, namely, static and free-range, by employing three synthetic mobility models (one

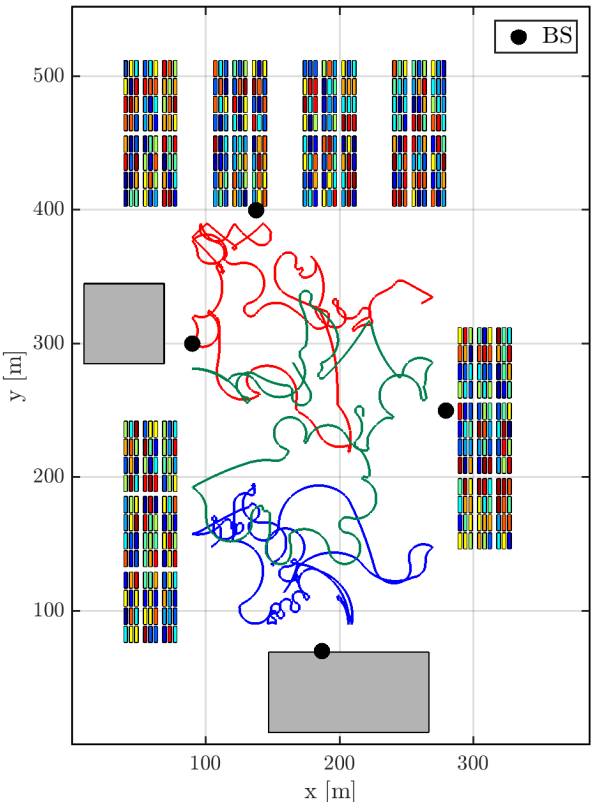

Fig. 3: Illustration of simulation layout for performance evaluation of proposed two-stage EKF positioning algorithm. In container port area, gray rectangles represent buildings and colored rectangles depict stocks of metal containers. Black circles correspond to BS positions, while UE trajectories are plotted as color curves. Radio channels between UEs and BSs are modeled according to METIS ray-tracing model [34].

TABLE III: Simulation Parameters

Parameter	Value
Central frequency	28 GHz*
Number of subcarriers	800
Subcarrier spacing	120 kHz**
NR slot duration	125 µs**
RS time interval	160 ms**
Bandwidth, W	96 MHz**
Number of UEs, K	3
Number of UE beams, $\mathcal{M}_{\mathrm{UE}}$	52
UE array coverage, azimuth, and elevation	(360°, 40°)
UE velocity ("fast"/"slow"), v	7 / 3 kmph*
UE height, h_{UE}	1.5 m*
Number of BSs, L	4
Number of BS beams, $\mathcal{M}_{\mathrm{BS}}$	64
BS orientation uncertainties, $\theta, \phi = \delta$	0°, 3°, 5°, 10°

* Evaluation parameters according to 3GPP TR 38.855
** Deployment parameters compatible with 3GPP TS 38.211, 38.213

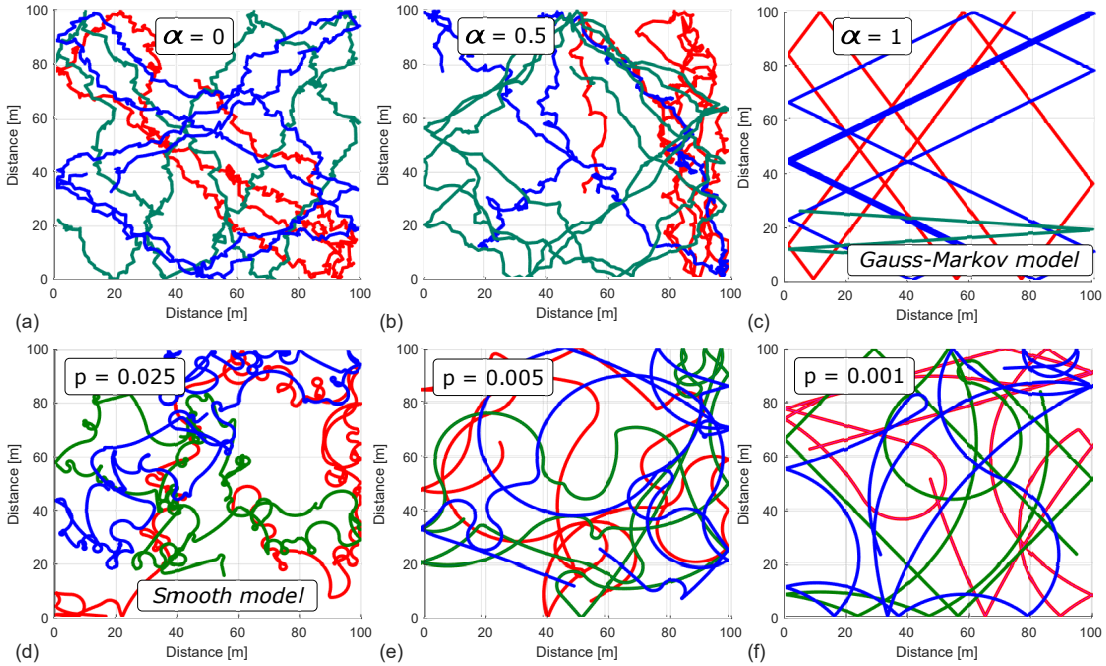

Fig. 4: Random trajectories (blue, red, green) generated by employed mobility models for varying parameters that control movement randomness. Subplots (a)-(c) correspond to Gauss-Markov mobility model and demonstrate different degrees of randomness by α: from Brownian motion (a) to linear mobility (c). Subplots (d)-(f) depict smooth mobility trajectories for varying parameter p.

deterministic and two random options) that characterize the two-dimensional motion of the UEs (UE antenna elevation h_{UE} is assumed to remain constant):

- *Rectilinear movement (static routing)* where machines move along the predetermined straight paths parallel to one of the axes.
- *Gauss-Markov mobility (free-range routing)* model [42], [43] where machine speeds and directions are correlated in time, while the degree of randomness is controlled by a single parameter, $\alpha \in [0, 1]$. In particular, $\alpha = 0$ corresponds to a memoryless process (Brownian motion) and $\alpha = 1$ represents strong process memory (that is, linear motion). Speed v_n and distance d_n at each discrete instant of time n can be established as:

$$\begin{aligned} v_n &= \alpha v_{n-1} + (1-\alpha)\overline{v} + \sqrt{(1-\alpha^2)w_{v_n}} \\ d_n &= \alpha d_{n-1} + (1-\alpha)\overline{d} + \sqrt{(1-\alpha^2)w_{d_n}}, \end{aligned} \tag{15}$$

  where v_{n-1}, d_{n-1} correspond to the previous time instant, $\overline{s}, \overline{d}$ are constants, and w_{v_n}, w_{d_n} are independent Gaussian random variables.
- *Discrete smooth mobility (free-range)* model that is constructed by analogy with the smooth mobility from [44], [45]. In this model, once per a time interval that is distributed geometrically with the parameter q_{DSM}, the AGV selects a new random direction. Then, the vehicle gradually rotates by incrementally changing its direction towards the target values, thus, avoiding unrealistic sharp turns.

We constrain all of our mobility trajectories by introducing bounces from the boundaries of the area of interest. We also note that the AGVs always face the direction of their movement and their antennas are tightly coupled with the solid body motion. Example trajectories for three devices in an arbitrary area of $100\,\mathrm{m} \times 100\,\mathrm{m}$ are illustrated in Fig. 4(a-c) and Fig. 4(d-f) for the Gauss-Markov and the smooth model, respectively.

B. Positioning and MAC-Layer Abstraction

Our joint framework for the co-design of networking and positioning comprises of two large blocks, "positioning" module and "system-level" module. While the former relies upon more detailed modeling and ray tracing, the latter mimics the MAC functionality, beamtraining, and data transmission. It aims at the estimation of the performance metrics, such as spectral efficiency, which is averaged over time, space, and the UEs.

To achieve encapsulation between the employed blocks, we abstract the details of the positioning algorithm by modeling its output (i.e., the resulting positioning error) as a random variable. In particular, we assume that the positioning errors follow a circular multivariate Gaussian distribution with the standard deviation of σ_{pos} and the zero correlation matrix. We have validated our abstraction by comparing its performance to the output of the setup with the full information; however, the details of that comparison are out of the main scope of this work. We emphasize that σ_{pos} may also serve as a quantitative measure of the positioning method, depending on the deployment geometry, UE speed, UE/BS antenna arrays, and the degree of uncertainty δ.

In our evaluation, we assume that each UE-BS pair may perform beamtraining with a certain periodicity of $\tau_{\mathbf{BF}}$ time slots. In our setup, the default beamtraining is conducted by using exhaustive search, i.e., the UEs are required to explore all of the available transmit and receive antenna configurations,

while the sought beams are selected based on the best received signal strength indicator (RSSI). Alternatively, if the positioning information is available, the beams are selected based on the estimated UE-BS alignment, while the beamtraining overhead is substantially reduced.

Therefore, we envision two potential options with respect to the availability of the positioning and tracking information:

1) *Proposed solution:* Using the positioning scheme devised and detailed in this work, the network estimates the UE location with the accuracy of σ_{pos}, compensates for the BS uncertainty, and then selects the appropriate mmW beams every τ time units. Importantly, the information on the direction of the BS antenna arrays may be distorted by an uncertainty component $\mathbf{a}'_{\text{BS}} = \mathbf{a}_{\text{BS}} + \Delta\mathbf{a}$, where $\mathbf{a}_{\text{BS}}$ is the exact direction that the mmW antenna array is inclined to, while $\Delta\mathbf{a}$ is a vector with the spherical coordinates of $(\pm\delta, \pm\delta, 1)$. Below, we refer to δ as to the degree of uncertainty.
2) *Comparison baseline:* The positioning information is unavailable at the BS; hence, the UE performs a straightforward brute-force search and updates the beam alignment information with the periodicity of $\tau_{\mathbf{BF}}$. In this case, by assuming no channel reciprocity, we calculate the beamtraining overhead proportionally to the number of the available UE and BS beams. The orientation uncertainly does not affect the results of the beamforming procedure by design.

The instantaneous data rate may then be obtained by using the Shannon's formula $\eta W \log(1+\text{SNR}) = \eta W \log(1+\frac{P_{\text{rx}}}{P_N})$, where P_N is the noise power, η is the share of radio resources after subtracting the beamtraining overheads (estimated according to the 5G NR timings, TTI, and frame structure), and P_{rx} is the receive power that can be derived as

$$P_{\text{rx}} = P_{\text{tx}} L^{-1}(d) G_{\text{UE}}(\Delta\varphi_{\text{UE}}, \Delta\vartheta_{\text{UE}}) G_{\text{BS}}(\Delta\varphi_{\text{BS}}, \Delta\vartheta_{\text{BS}}), \tag{16}$$

where $L(d) = \left(\frac{4\pi d}{\lambda}\right)^2$ is the path loss for a LoS-link at the distance of d meters, while $G_{\text{UE}}(\Delta\varphi_{\text{UE}}, \Delta\vartheta_{\text{UE}})$ and $G_{\text{BS}}(\Delta\varphi_{\text{BS}}, \Delta\vartheta_{\text{BS}})$ are the antenna gains at the UE and the BS, given the respective antenna misalignment $\Delta\varphi_{.}, \Delta\vartheta_{.}$.

The BS transmit power P_{tx} is fixed across the entire network. The gains are calculated based on the information about the antenna array direction, the selected beams, the directions to the UE/BS, and the initial/developed beam misalignment. Importantly, we require that the BSs employ 5G-grade interference coordination mechanisms; hence, one may assume noise-limited operation.

V. Numerical Results

In this section, we present the results of our numerical evaluation and analyze the impact of positioning accuracy on the system-level performance.

A. Positioning Algorithm Evaluation

We begin with evaluating the impact of user mobility and network parameters on the performance of the proposed solution. We rely upon the combined results of the steady-state EKF operation for a large number of trajectories that follow smooth user mobility. In this subsection, we target two metrics: (i) the absolute error for the horizontal positioning and (ii) the standard deviation of the UE positioning error, σ_{pos} (see Section IV-B). We particularly focus on the horizontal positioning since the UE antenna elevation remains constant when users move predominantly in the horizontal plane. To this end, we adjust the second-stage-EKF state noise covariance matrix by increasing the positioning error margin in the x- and y-dimensions and decreasing it in the z-dimension. We note that the proposed positioning algorithm, by its design, is not limited to horizontal mobility and can be configured according to another desired use case.

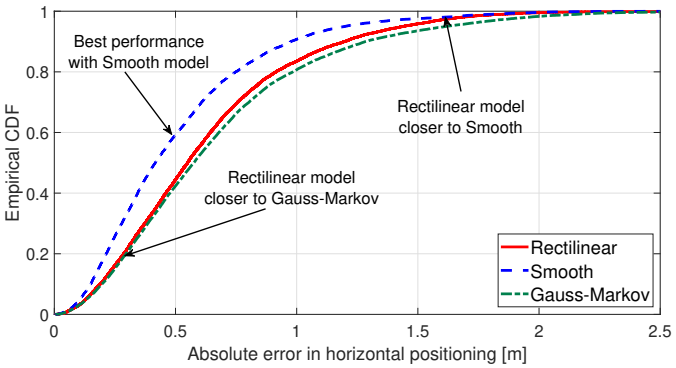

Fig. 5: Horizontal positioning accuracy for three mobility models: Rectilinear, Gauss-Markov, and Smooth Mobility; "slow" scenario ($v = 3$ kmph). Orientation uncertainty is not introduced.

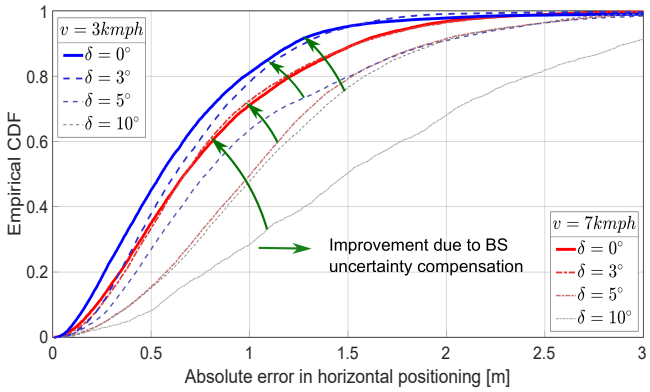

Fig. 6: Absolute error in horizontal positioning for smooth mobility model with $v = 3$ kmph (blue curve) and 7 kmph (red curve), for perfect alignment (solid line), and for different example values of the orientation uncertainty (dashed lines). Note that this performance is for the case of *uncompensated orientation uncertainty*. Green arrows highlight potential improvement if estimated value of orientation uncertainty is used to compensate the BS antenna misalignment.

1) Comparison of positioning performance for different mobility models: First, we compare the positioning performance for the three mobility models as outlined in Section IV-A. In particular, Fig. 5 illustrates the cumulative distribution functions (CDFs) of the horizontal positioning accuracy for the three cases: rectilinear, smooth ($p \in [0.006 - 0.01]$), and Gauss-Markov ($\alpha = 0.3$) under zero orientation uncertainty. While for the Gauss-Markov model the position estimation accuracy is the lowest, our positioning algorithm slightly improves the respective performance in the case of the rectilinear model and *achieves the best accuracy in the case of the smooth mobility trajectories*. This result may be attributed to the distribution

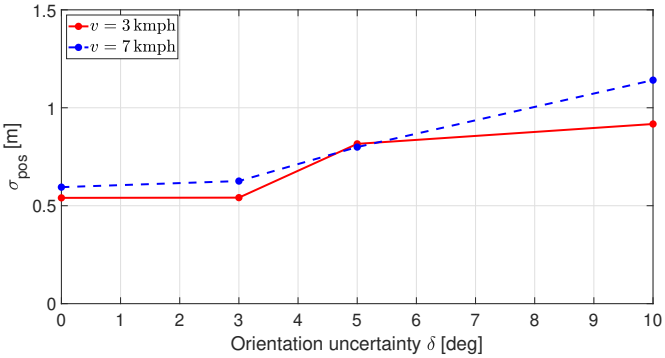

Fig. 7: Empirical values of σ_{pos} with $v = 3$ kmph and 7 kmph under smooth mobility model for different values of the orientation uncertainty.

of the UE locations along different trajectories as well as to the changes in UE orientation due to the motion pattern.

The Gauss-Markov mobility model produces trajectories with rapid changes of the motion direction. Hence, the UE heading angles alter abruptly, which causes DoD tracking errors and results in reduced positioning accuracy. We conclude that in the considered scenario, first- and second-stage EKFs limit the performance of the positioning algorithm in the cases of rectilinear and Gauss-Markov mobility. However, for a *more realistic smooth mobility model* and the velocity of $v = 3$ kmph, our positioning algorithm *reaches sub-meter accuracy with* 90% *availability*.

Interestingly, the rectilinear mobility model is comparable to the Gauss-Markov case for about 40% of the most accurate locations. However, for 5% of the least accurate locations, its behavior remains closer to the smooth mobility model, which is due to the similarity of the rectilinear and the Gauss-Markov options for larger values of α. Here, we emphasize that especially for the values of parameter $\alpha \geq 0.5$ (see Fig. 4), Gauss-Markov trajectories resemble a set of linear trajectories with abrupt changes of the moving direction at the boundaries. This somewhat reduces the positioning accuracy for certain locations but does not introduce significantly higher errors, as confirmed by the absence of a heavy tail in the CDF.

2) Joint estimation of position and orientation uncertainty: We continue by studying the dependence of the second-stage EKF estimation accuracy on the orientation uncertainty for a smooth UE mobility and the velocities $v = 3$ kmph (a "slow" user) and $v = 7$ kmph (a "fast" user). Orientation uncertainties in the azimuth and the co-elevation direction are introduced to all of the BSs, and then estimated and tracked alongside the position of the UE. For the sake of simplicity, the values of θ and ϕ are chosen as $(\theta, \phi) = (\pm\delta, \pm\delta)$, where $\delta = 3°, 5°, 10°$, while the sign is set randomly; the baseline value is $\delta = 0°$ (no orientation uncertainty). We remind that the proposed algorithm performs best for smaller orientation uncertainties of $\delta \leq 5°$. However, to explore its applicability limits, we also include $\delta = 10°$ as part of our analysis.

The introduced orientation uncertainty *decreases the accuracy of positioning*, as can be concluded based on the CDF plots in Fig. 6. The positioning accuracy also *depends on the UE speed*; however, for the selected parameters, its impact is marginal. For example, for the UE velocity of $v = 3$ kmph,

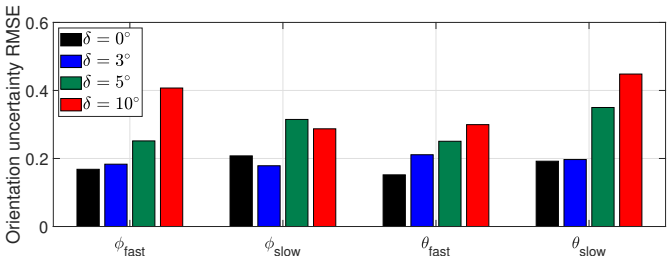

Fig. 8: Performance of orientation uncertainty estimation for smooth mobility model, $v = 3$ kmph ("slow") and $v = 7$ kmph ("fast"): bar plot of orientation uncertainty RMSE in elevation (θ) and azimuth (ϕ) for $\delta = 0°, 3°, 5°, 10°$.

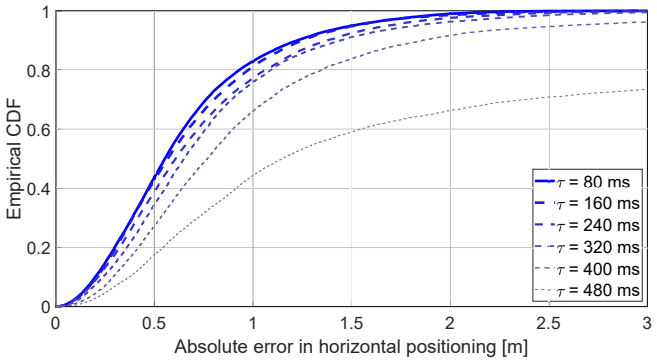

Fig. 9: Absolute error in horizontal positioning for different values of BRSRP measurement interval $\tau = [80, 480]$ ms, $v = 7$ kmph.

the effect of $\Delta\delta = 5°$ substantially exceeds the influence of $\Delta v = 4$ kmph. In Fig. 7, we explore the dependence of the standard deviation of the positioning error, σ_{pos} (as detailed in Section IV-B), on the orientation uncertainty, δ. Notably, for lower uncertainties $\phi, \theta = \delta \leq 3°$, σ_{pos} remains stable, marginally increasing within the range $3° \leq \delta \leq 5°$.

The absolute accuracy of the orientation uncertainty estimation *decreases with the actual value of the orientation uncertainty* δ, as can be confirmed in Fig. 8. The bar plot presents the root-mean-squared errors (RMSEs) of the orientation uncertainty estimation. Notably, the impact of smaller orientation uncertainties $\delta \leq 3°$ is negligible. Further visual illustrations of the positioning and orientation estimation accuracy are available in the form of the supplementary multimedia materials accompanying this contribution (also available here for readers' convenience).

We emphasize that the presented performance results assume that the system with the BS orientation misalignment does not utilize any feedback for correction purposes. In other words, the orientation uncertainty is *estimated, but not compensated*. Since the orientation uncertainty is expected to remain static (or change slowly), the network can estimate its value for a limited time and then employ the obtained estimate to improve the BS orientation knowledge. Then, for the compensated BS orientation, $(|\theta|, |\phi|) \lessapprox (0.4°, 0.4°)$ (see Fig. 8). In this case, the *positioning performance is essentially equivalent to that without orientation uncertainty.* We indicate the potential improvement in the positioning performance by the green arrows in Fig. 6 and also later with green bars in Fig. 12.

3) Comparison of positioning performance for different durations of RS measurement period: Finally, we analyze the positioning accuracy as a function of the BRSRP measurements period τ in Fig. 9. The performance degrades very mildly

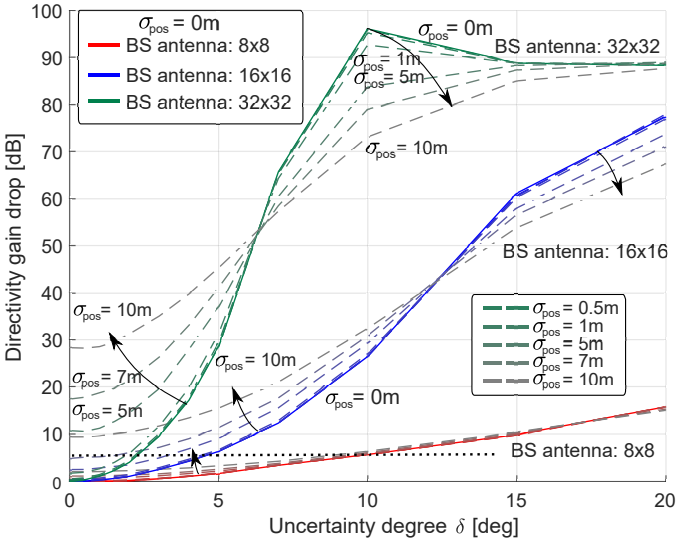

Fig. 10: Illustration of the decrease in the total antenna directivity $G_{\text{tx}} + G_{\text{rx}}$ due to beam misalignment for three uniform rectangular antenna arrays: 8×8 (red), 16×16 (blue), and 32×32 (green). Ideal information on UE locations corresponds to solid lines $\sigma_{\text{pos}} = 0$, while gradients (dashed lines) illustrate the effect of increased positioning inaccuracy $\sigma_{\text{pos}} > 0$.

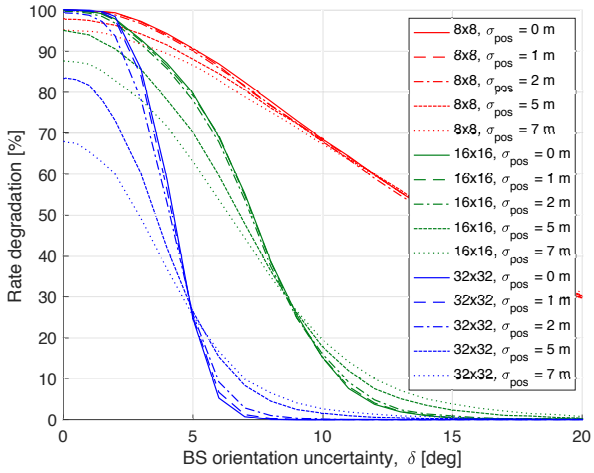

Fig. 11: Impact of positioning (σ_{pos}) and orientation (δ) uncertainties on share of achievable UE data rate w.r.t. ideal scenario for three uniform rectangular antenna arrays: 8x8 (red), 16x16 (green), and 32x32 (blue).

for the values of τ between $80\,\text{ms}$ and $320\,\text{ms}$. Hence, we may increase the periodicity of the BRSRP measurements and the EKF updates *to reduce the overheads without loss in the positioning performance*. We note that in terms of the resulting positioning performance, the scaling of τ is identical to the velocity scaling. For example, the degradation of the positioning performance for $\tau = 320\,\text{ms}$ with respect to $\tau = 160\,\text{ms}$ is equivalent to the case where the velocity is varied from $v = 7\,\text{kmph}$ to $v = 14\,\text{kmph}$.

B. Connectivity Impact of Positioning and Orientation Inaccuracy

1) Effects on directivity gain and instantaneous data rate: Assuming positioning-based beamforming, we continue by evaluating synthetically the effects of both σ_{pos} and uncompensated orientation uncertainty, δ, on the connectivity between the UE and the BS. In Fig. 10, we provide the results of our simulation study for three realistic BS antenna patterns derived in Phased Array MATLAB toolbox – namely, uniform rectangular arrays of 8×8 (solid red curve for ideal positioning σ_{pos}), 16×16 (blue), and 32×32 (green) antenna elements. The UE antenna pattern is obtained similarly but as a uniform linear array of 4 elements.

Specifically, in Fig. 10, we assess the change in the total directivity gain $G_{\text{tx}} + G_{\text{rx}}$ after introducing the positioning (x-axis) and the uncompensated orientation uncertainty (dashed curves with faded color for increased σ_{pos}). Naturally, wider antenna beams are more robust to both degrees of uncertainty, while narrower ones demonstrate unstable behavior over almost the entire range of σ_{pos}. However, as demonstrated in the previous subsection, the proposed estimation scheme results in the positioning error values of below $3\,\text{m}$ (see Fig. 6), which *may support even very narrow beams if δ is sufficiently small*, as in the lower-left corner of the plot. Interestingly, the trend of increased directivity loss with decreased positioning uncertainty changes to the opposite situation as the orientation uncertainty grows for a fixed antenna design. This effect can be attributed to mutual compensation of the two uncertainties; however, it becomes negligible as the antenna beam widens as can be observed from the group of red curves.

Further, Fig. 11 highlights the impact of the considered uncertainties on the degradation in the instantaneous data rate that occurs due to mmW beam misalignment. Here, we assume $400\,\text{MHz}$ channel with the noise power of $-88\,\text{dBm}$. We vary the BS antenna beamwidth by considering the uniform rectangular antenna arrays of 8×8 (the group of red curves), 16×16 (green color), and 32×32 (blue) antenna elements. We observe that the narrowest beams are prone to the most severe data rate degradation, and the *uncertainty δ in the orientation (the steeper slope) plays a more significant role* than the precision of the positioning algorithm. We note that the use of narrower beams entails faster decrease in the data rate, which may rapidly lead to near-zero data rates if the accuracy drops. However, our proposed approach yields the uncertainty of less than $1°$, as shown in Fig. 7. Therefore, it can be reliably applied in the settings with *narrower beams*. The use of highly directional antennas being supported by our solution may thus significantly improve the coverage and the spatial reuse in mmW networks without excessive beamforming overheads.

2) Comparison with conventional beamforming: Finally, we employ the smooth mobility model to capture the temporal dynamics of the mmW network operation. To illustrate the impact of our solution on the system spectral efficiency, we compare the results of (i) the proposed algorithm in the case of zero or compensated BS orientation uncertainty (residual uncertainty $\delta = 0°$, solid green line) and (ii) our positioning algorithm with the positioning accuracy as shown in Fig. 7, but uncompensated BS uncertainty (dashed and dotted green lines for $\delta = 5°$ and $\delta = 10°$, correspondingly). In addition, we provide the spectral efficiency of the conventional beamforming scheme (blue line), where we assume brute-force

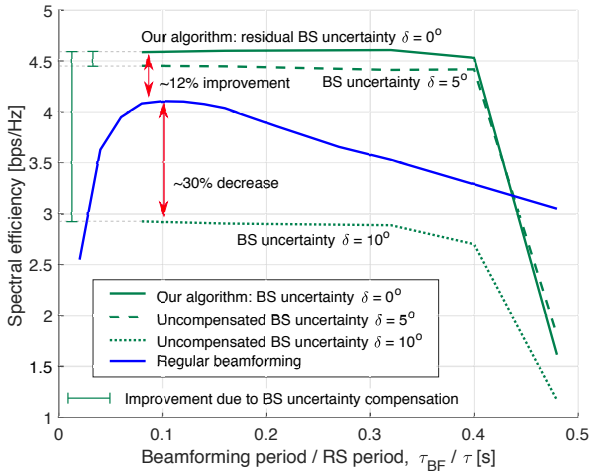

Fig. 12: Comparison of our proposed scheme against conventional brute-force beam-search for varying beam update periods τ_{BF} (conventional BF, blue) and τ (proposed position-based BF, green), $v = 7$ kmph. The performance of positioning-based beamforming system is shown and indicated without and with BS orientation uncertainty compensation.

beam-search with the signaling overheads based on the 3GPP recommendations for the mmW system operation [46].

As reported in Fig. 12, the heavy overhead incurred by the beamtraining for both transmit and receive beams results in decreased data rates as the beamforming (BF) or beam-update period τ_{BF} shortens. On the other hand, the increased period between the consecutive beamtraining procedures leads to a dramatic data rate degradation due to the high mobility of the UEs. As a result, traditional beamforming schemes may have an optimum point that maximizes the network performance by selecting the best τ_{BF}. However, the performance of our proposed scheme *exceeds this upper bound for the conventional beamforming training by more than* 10% when orientation uncertainty compensation is applied. Even in the case of higher uncompensated orientation uncertainty of $\delta = 5°$, our solution demonstrates better performance than the conventional beam-search. Finally, in the extreme case of $\delta = 10°$, the position-based BF approach is clearly compromised, if the orientation uncertainty is not compensated for.

In the selected setup, the proposed solution improves the system-level performance if the period τ remains within the interval $[0, 400]$ ms, unless a very large uncompensated orientation uncertainty is present. Beamforming mechanisms based on other positioning solutions may also bring noticeable benefits at the system level, if the BS orientation uncertainty remains reasonably small (that is, less than $5°$ in our example). Otherwise, if the uncertainty increases to the levels that the employed positioning and orientation estimation algorithm cannot account for, conventional beamforming mechanisms could become more efficient. We emphasize that the addressed baseline suffers from the highest overhead, and there exist more complex and dynamic beamtraining solutions. However, more sophisticated beamforming procedures might be sensitive to the modeling environment and, thus, become less predictable.

VI. Conclusion

Since multi-connectivity is being recognized as a key solution to combat the unreliability of highly directional mmW connections, simplifying the UE antenna system and beamforming coordination complexity becomes vital for maintaining efficient network performance. To reduce the beamforming overheads, the mmW system can rely on accurate and timely information regarding the device locations. Today, various positioning schemes may already exploit the flexible numerology of the latest 5G NR specifications and be designed within the actual protocol structure, e.g., by utilizing the existing 5G NR reference signals (RSs) in a typical multi-connectivity setup.

In this work, we developed a flexible and scalable framework for the co-design of mmW networking and positioning in a system with the multi-connectivity capabilities. Our proposed solution enables unassisted, DoD-based, and high-accuracy 3D user positioning and tracking in 5G NR deployments with simultaneous estimation of the BS orientation uncertainty in 3D space. The proposed approach employs measurements of the beam pair based RSRPs and remains flexible with respect to the actual structure of the utilized reference signals.

We confirmed that our proposed positioning framework is capable of performing accurately under complex, random, or time-correlated device mobility as well as can yield the positioning inaccuracies that are sufficiently low to support even very narrow mmW beams, e.g., those having the horizontal and vertical half-power beamwidth in the order of $5°$. The possibility of tracking such extremely narrow beams may significantly improve the coverage and the spatial reuse in 5G-and-beyond mmW systems, thus, reflecting the features that are difficult or costly to achieve without the use of appropriate positioning algorithms embedded into the existing network architecture.

Importantly, we also established that for the small-scale BS orientation uncertainties, the proposed positioning scheme outperforms the upper bound on the conventional brute-force beam-training based beamforming by 10% in terms of the data rate. In the case of higher inaccuracies, our algorithm can estimate and, therefore, help compensate the associated discrepancy. Hence, it should deliver better performance and reliability than those offered by the more conventional brute-force type beamforming methods. Hence, we conclude that the proposed method and our overall framework provide a notable contribution toward the true co-design of networking and positioning in prospective mmW networks with multi-connectivity operation.

Appendix
Derivation of Stage 1 DoD-EKF

It can be shown [47] that the BRSRP measurements (2) in a LoS-dominated channel follow a non-central χ^2-distribution with $2\mathcal{M}_f$ degrees of freedom. The corresponding probability density function (PDF) is given by [48, Ch.2]:

$$p(\beta_{i,j}) = \frac{\mathcal{M}_f}{\tilde{\sigma}^2_{i,j}} \left(\frac{\mathcal{M}_f \beta_{i,j}}{\lambda_{i,j}} \right)^{\frac{\mathcal{M}_f - 1}{2}} \mathrm{e}^{-\frac{\lambda_{i,j} + \mathcal{M}_f \beta_{i,j}}{\tilde{\sigma}^2_{i,j}}} \times I_{\mathcal{M}_f - 1} \left(\frac{2\sqrt{\lambda_{i,j} \mathcal{M}_f \beta_{i,j}}}{\tilde{\sigma}^2_{i,j}} \right), \tag{17}$$

where $\tilde{\sigma}^2_{i,j}$ is the BRSRP measurement noise variance and $I_x(\cdot) \in \mathbb{R}$ denotes a modified Bessel function of the first kind, and the non-centrality parameter is proportional to the received signal power:

$$\lambda_{i,j} = \sum_{m=1}^{\mathcal{M}_f} |[\boldsymbol{S}]_m [\boldsymbol{b}_f]_m b^i_{\mathrm{UE}}(\vartheta_a, \varphi_a) b^j_{\mathrm{BS}}(\vartheta_d, \varphi_d) \gamma_{i,j}|^2. \quad (18)$$

The measurement noise between the ith UE beam and the jth BS beam is a complex circular Gaussian random variable $\boldsymbol{n}_{i,j} \sim \mathcal{N}_C(\boldsymbol{0}, \tilde{\sigma}^2_{i,j}\boldsymbol{I}) \in \mathbb{C}^{\mathcal{M}_f}$. We also assume that the noise is uncorrelated for different beam pairs, i.e., $\mathbb{E}\{\boldsymbol{n}_{i,j}\boldsymbol{n}^H_{k,l}\} = \boldsymbol{0}$ where $i \neq k$ or $j \neq l$, while the variances are identical for all the beam-pairs $\tilde{\sigma}^2_{i,j} = \tilde{\sigma}^2, \forall(i,j)$.

For a large number of subcarriers, $\mathcal{M}_f$, (17) converges to a Gaussian distribution [47]; hence, $\beta_{i,j} \sim \mathcal{N}(\mu_{i,j}, \sigma^2_{i,j})$, with the mean and variance of the BRSRP measurements given by

$$\mu_{i,j} = \frac{\lambda_{i,j}}{\mathcal{M}_f} + \tilde{\sigma}^2_{i,j} \quad (19)$$

$$\sigma^2_{i,j} = \frac{\tilde{\sigma}^4_{i,j}}{\mathcal{M}_f} + \frac{2\tilde{\sigma}^2_{i,j}\lambda_{i,j}}{\mathcal{M}^2_f}. \quad (20)$$

At the third step of the positioning Algorithm 1, each UE selects the Rx beam corresponding to the largest sum of the BRSRP measurements over all of the Tx BS beams: $\max_i \sum_{j=1}^{\mathcal{M}_{\mathrm{BS}}} \beta_{i,j}$. Let us denote the vector containing the BRSRP measurements for all of the BS beams and the chosen UE beam as $\boldsymbol{\beta} \in \mathbb{R}^{\mathcal{M}_{\mathrm{BS}}}$. Hence, $\boldsymbol{\beta} \sim \mathcal{N}(\boldsymbol{\mu}(\boldsymbol{\Theta}), \boldsymbol{C}(\boldsymbol{\Theta}))$, where the mean and the covariance matrix can be expressed as follows:

$$\boldsymbol{\mu}(\boldsymbol{\Theta}) = \boldsymbol{a}(\vartheta_d, \varphi_d)\rho\frac{P_{\mathrm{Tx}}}{\mathcal{M}_f} + \boldsymbol{1}\tilde{\sigma}^2 \quad (21)$$

$$\boldsymbol{C}(\boldsymbol{\Theta}) = \mathrm{diag}\left\{\boldsymbol{a}(\vartheta_d, \varphi_d)\rho\frac{2\tilde{\sigma}^2 P_{\mathrm{Tx}}}{\mathcal{M}^2_f} + \boldsymbol{1}\frac{\tilde{\sigma}^4}{\mathcal{M}_f}\right\}, \quad (22)$$

where $\boldsymbol{\Theta} = [\vartheta_d, \varphi_d, \rho, \tilde{\sigma}^2]^{\mathrm{T}}$ is the vector of unknown parameters: (ϑ_d, φ_d) is the DoD azimuth and co-elevation angles, while $\rho = |\boldsymbol{b}^i_{\mathrm{UE}}(\vartheta_a, \varphi_a)|^2|\gamma_{i,j}|^2 \in \mathbb{R}$ is related to the user beam pattern $\boldsymbol{b}^i_{\mathrm{UE}}$ and the path weight $\gamma_{i,j}$. Moreover, $P_{\mathrm{Tx}} = \sum_{m=1}^{\mathcal{M}_f} |[\boldsymbol{S}]_m[\boldsymbol{b}_f]_m|^2$, and $\boldsymbol{a}(\vartheta_d, \varphi_d) \in \mathbb{C}^{\mathcal{M}_{\mathrm{BS}}}$ is given by

$$\boldsymbol{a}(\vartheta_d, \varphi_d) = \left[\left|\boldsymbol{b}^1_{\mathrm{BS}}(\vartheta_d, \varphi_d)\right|^2, \ldots, \left|\boldsymbol{b}^{\mathcal{M}_{\mathrm{BS}}}_{\mathrm{BS}}(\vartheta_d, \varphi_d)\right|^2\right]^{\mathrm{T}}. \quad (23)$$

The received signal-to-noise ratio (SNR) of the beam pair (i,j) can be expressed in terms of the original distribution parameters as

$$\mathrm{SNR}_{i,j} \triangleq \frac{\lambda_{i,j}}{\mathcal{M}_f\tilde{\sigma}^2_{i,j}}. \quad (24)$$

We consider the low-SNR regime, where $\mathcal{M}_f\tilde{\sigma}^2_{i,j} > \lambda_{i,j}$ and assume the covariance of $\boldsymbol{\beta}$ to be independent of the DoD. In the case of unknown BSs orientation uncertainty (θ, ϕ), the first-stage DoD estimates are biased; however, our assumption remains valid for the values of (θ, ϕ) that do not exceed the BS beamwidth. Hence, the resulting log-likelihood function has the following form:

$$\begin{aligned}\ell_{\mathrm{aprx}}(\boldsymbol{\Theta}, \sigma^2|\boldsymbol{\beta}) = &-\frac{\mathcal{M}_{\mathrm{BS}}}{2}\ln 2\pi - \frac{\mathcal{M}_{\mathrm{BS}}}{2}\ln\sigma^2 \\ &- \frac{1}{2\sigma^2}\|\boldsymbol{\beta} - \boldsymbol{\mu}(\boldsymbol{\Theta}))\|^2.\end{aligned} \quad (25)$$

This expression is separable with respect to the DoDs(ϑ_d, φ_d) and other unknown parameters $(\boldsymbol{\rho}, \tilde{\sigma}^2, \sigma^2)$. The maximum likelihood estimators (MLEs) of $\boldsymbol{\rho}$, $\tilde{\sigma}^2$, and σ^2 can be established in the closed-form for a given (ϑ, φ) [49], [50] as

$$\begin{aligned}\begin{bmatrix}\hat{\rho}\\ \hat{\tilde{\sigma}}^2\end{bmatrix} &= \left[\boldsymbol{a}(\vartheta_d, \varphi_d)\frac{P_{\mathrm{Tx}}}{\mathcal{M}_f}, \boldsymbol{1}\right]^{\dagger}\boldsymbol{\beta} \\ \hat{\sigma}^2 &= \frac{1}{\mathcal{M}_{\mathrm{BS}}}\|\boldsymbol{P}^{\perp}_{a1}(\vartheta_d, \varphi_d)\boldsymbol{\beta}\|^2,\end{aligned} \quad (26)$$

with $(\cdot)^{\dagger}$ denoting the Moore-Penrose pseudo-inverse operator. Here, $\boldsymbol{P}_{a1}(\vartheta_d, \varphi_d) \in \mathbb{R}^{\mathcal{M}_{\mathrm{BS}} \times \mathcal{M}_{\mathrm{BS}}}$ is the orthogonal projection matrix and $\boldsymbol{P}^{\perp}_{a1}(\vartheta_d, \varphi_d) = \boldsymbol{I} - \boldsymbol{P}_{a1}(\vartheta_d, \varphi_d)$ is an orthogonal projection onto a null-space of $\boldsymbol{P}_{a1}(\vartheta_d, \varphi_d)$. Further, $\boldsymbol{P}_{a1}(\vartheta_d, \varphi_d) = \boldsymbol{\mathcal{P}}_a(\vartheta_d, \varphi_d) + \boldsymbol{\mathcal{P}}_1$, where $\boldsymbol{\mathcal{P}}_a(\vartheta_d, \varphi_d)$ and $\boldsymbol{\mathcal{P}}_1$ are the oblique projection matrices. In particular, the range of $\boldsymbol{\mathcal{P}}_a(\vartheta_d, \varphi_d)$ is $Span(\boldsymbol{a}(\vartheta_d, \varphi_d))$ and its null-space is $Span(\boldsymbol{1})$. Conversely, the range of $\boldsymbol{\mathcal{P}}_1$ is $Span(\boldsymbol{1})$, while its null-space is $Span(\boldsymbol{a}(\vartheta_d, \varphi_d))$ [51].

The above MLEs (26) can be substituted into (25) to obtain the concentrated log-likelihood function:

$$\begin{aligned}\ell_{\mathrm{caprx}}(\vartheta_d, \varphi_d|\boldsymbol{\beta}) = &-\frac{\mathcal{M}_{\mathrm{BS}}}{2}\ln 2\pi - \frac{\mathcal{M}_{\mathrm{BS}}}{2} \\ &- \frac{\mathcal{M}_{\mathrm{BS}}}{2}\ln\frac{\|\boldsymbol{P}^{\perp}_{a1}(\vartheta_d, \varphi_d)\boldsymbol{\beta}\|^2}{\mathcal{M}_{\mathrm{BS}}}.\end{aligned} \quad (27)$$

We choose the information form of EKF, where the covariance of the state in (4) is updated by using the observed FIM and the gradient of the log-likelihood function (27). The expression for the log-likelihood function in the case of the Gaussian distribution can be found in [33, Ch.3]. For the employed approximations, the gradient and the observed FIM (or Hessian) for the concentrated log-likelihood function follow from the results provided in [52], [53].

For convenience, instead of the concentrated log-likelihood function, we utilize its exponent $\exp\{\ell_{\mathrm{caprx}}(\vartheta_d, \varphi_d|\boldsymbol{\beta})\}$, which does not change the location of the global maximum. The gradient of the said exponent with respect to the azimuth and the co-elevation directions can be expressed as

$$\begin{aligned}[\boldsymbol{q}(\vartheta_d, \varphi_d)]_1 &= 2\left(\frac{\partial}{\partial\vartheta_d}\boldsymbol{P}^{\perp}_{a1}(\vartheta_d, \varphi_d)\,\boldsymbol{\beta}\right)^{\mathrm{T}}\boldsymbol{P}^{\perp}_{a1}(\vartheta_d, \varphi_d)\,\boldsymbol{\beta} \\ [\boldsymbol{q}(\vartheta_d, \varphi_d)]_2 &= 2\left(\frac{\partial}{\partial\varphi_d}\boldsymbol{P}^{\perp}_{a1}(\vartheta_d, \varphi_d)\,\boldsymbol{\beta}\right)^{\mathrm{T}}\boldsymbol{P}^{\perp}_{a1}(\vartheta_d, \varphi_d)\,\boldsymbol{\beta},\end{aligned} \quad (28)$$

while the first-order approximation of the FIM has the following form:

$$\begin{aligned}[\boldsymbol{\mathcal{I}}(\vartheta_d, \varphi_d)]_{1,2} \approx 2&\left(\frac{\partial}{\partial\vartheta_d}\boldsymbol{P}^{\perp}_{a1}(\vartheta_d, \varphi_d)\,\boldsymbol{\beta}\right)^{\mathrm{T}} \\ &\times \frac{\partial}{\partial\varphi_d}\boldsymbol{P}^{\perp}_{a1}(\vartheta_d, \varphi_d)\,\boldsymbol{\beta},\end{aligned} \quad (29)$$

which offers better convergence [53].

REFERENCES

[1] K. David and H. Berndt, "6G Vision and Requirements: Is There Any Need for Beyond 5G?" *IEEE Vehicular Technology Magazine*, vol. 13, no. 3, pp. 72–80, Sep. 2018.

[2] H. Xu, W. Yu, D. Griffith, and N. Golmie, "A survey on industrial internet of things: A cyber-physical systems perspective," *IEEE Access*, vol. 6, pp. 78 238–78 259, 2018.

[3] M. Giordani, M. Polese, M. Mezzavilla, S. Rangan, and M. Zorzi, "Towards 6G networks: Use cases and technologies," 2019, arXiv:1903.12216.

[4] M. Luvisotto, Z. Pang, and D. Dzung, "High-performance wireless networks for industrial control applications: New targets and feasibility," *Proc. IEEE*, pp. 1–20, 2019.

[5] J. G. Andrews, T. Bai, M. N. Kulkarni, A. Alkhateeb, A. K. Gupta, and R. W. Heath, "Modeling and analyzing millimeter wave cellular systems," *IEEE Trans. Commun.*, vol. 65, no. 1, pp. 403–430, 2017.

[6] C. Slezak, V. Semkin, S. Andreev, Y. Koucheryavy, and S. Rangan, "Empirical effects of dynamic human-body blockage in 60 GHz communications," *IEEE Commun. Mag.*, vol. 56, no. 12, pp. 60–66, 2018.

[7] M. Rebato, J. Park, P. Popovski, E. De Carvalho, and M. Zorzi, "Stochastic geometric coverage analysis in mmWave cellular networks with realistic channel and antenna radiation models," *IEEE Trans. Commun.*, no. 5137, 2019.

[8] H. Shokri-Ghadikolaei, C. Fischione, G. Fodor, P. Popovski, and M. Zorzi, "Millimeter wave cellular networks: A MAC layer perspective," *IEEE Trans. Commun.*, vol. 63, no. 10, pp. 3437–3458, 2015.

[9] Y. Li, J. G. Andrews, F. Baccelli, T. D. Novlan, and C. J. Zhang, "Design and analysis of initial access in millimeter wave cellular networks," *IEEE Trans. Wireless Commun.*, vol. 16, no. 10, pp. 6409–6425, 2017.

[10] M. Mezzavilla, M. Zhang, M. Polese, R. Ford, S. Dutta, S. Rangan, and M. Zorzi, "End-to-end simulation of 5G mmWave networks," *IEEE Commun. Surveys Tuts.*, vol. 20, no. 3, pp. 2237–2263, 2018.

[11] M. Gerasimenko, D. Moltchanov, M. Gapeyenko, S. Andreev, and Y. Koucheryavy, "Capacity of multiconnectivity mmWave systems with dynamic blockage and directional antennas," *IEEE Trans. Veh. Technol.*, vol. 68, no. 4, pp. 3534–3549, 2019.

[12] M. Giordani, M. Mezzavilla, S. Rangan, and M. Zorzi, "An efficient uplink multi-connectivity scheme for 5G millimeter-wave control plane applications," *IEEE Trans. Wireless Commun.*, vol. 17, no. 10, pp. 6806–6821, 2018.

[13] V. Petrov, D. Solomitckii, A. Samuylov, M. A. Lema, M. Gapeyenko, D. Moltchanov, S. Andreev, V. Naumov, K. Samouylov, M. Dohler, and Y. Koucheryavy, "Dynamic multi-connectivity performance in ultra-dense urban mmWave deployments," *IEEE J. Sel. Areas Commun.*, vol. 35, no. 9, pp. 2038–2055, 2017.

[14] J. Talvitie, T. Levanen, M. Koivisto, K. Pajukoski, M. Renfors, and M. Valkama, "Positioning of high-speed trains using 5G new radio synchronization signals," in *IEEE Wireless Commun. and Networking Conf. (WCNC)*, Apr. 2018, pp. 1–6.

[15] H. Wymeersch, G. Seco-Granados, G. Destino, D. Dardari, and F. Tufvesson, "5G mmWave positioning for vehicular networks," *IEEE Wireless Commun.*, vol. 24, no. 6, pp. 80–86, Dec 2017.

[16] A. Dammann, R. Raulefs, and S. Zhang, "On prospects of positioning in 5G," in *2015 IEEE Int. Conf. Commun. Workshop (ICCW)*. IEEE, 2015, pp. 1207–1213.

[17] X. Cui, T. A. Gulliver, J. Li, and H. Zhang, "Vehicle positioning using 5G millimeter-wave systems," *IEEE Access*, vol. 4, pp. 6964–6973, 2016.

[18] J. Saloranta, G. Destino, A. Tölli, and H. Wymeersch, "Novel solution for multi-connectivity 5G-mmW positioning," in *52nd Asilomar Conf. Signals, Systems, and Computers*, 10 2018, pp. 537–540.

[19] R. Di Taranto and H. Wymeersch, "Simultaneous routing and power allocation using location information," in *2013 Asilomar Conf. Signals, Systems and Computers*. IEEE, 2013, pp. 1700–1704.

[20] R. Di Taranto, S. Muppirisetty, R. Raulefs, D. Slock, T. Svensson, and H. Wymeersch, "Location-aware communications for 5G networks: How location information can improve scalability, latency, and robustness of 5G," *IEEE Signal Processing Magazine*, vol. 31, no. 6, pp. 102–112, 2014.

[21] M. Koivisto, A. Hakkarainen, M. Costa, P. Kela, K. Leppänen, and M. Valkama, "High-efficiency device positioning and location-aware communications in dense 5G networks," *IEEE Communications Magazine*, vol. 55, no. 8, pp. 188–195, 2017.

[22] A. Shahmansoori, G. E. Garcia, G. Destino, G. Seco-Granados, and H. Wymeersch, "Position and orientation estimation through millimeter-wave MIMO in 5G systems," *IEEE Transactions on Wireless Communications*, vol. 17, no. 3, pp. 1822–1835, 2018.

[23] J. D. Roth, M. Tummala, and J. C. McEachen, "Fundamental implications for location accuracy in ultra-dense 5G cellular networks," *IEEE Transactions on Vehicular Technology*, vol. 68, no. 2, pp. 1784–1795, Feb 2019.

[24] J. A. del Peral-Rosado, G. Seco-Granados, S. Kim, and J. A. López-Salcedo, "Network design for accurate vehicle localization," *IEEE Transactions on Vehicular Technology*, vol. 68, no. 5, pp. 4316–4327, May 2019.

[25] E. Rastorgueva-Foi, M. Costa, M. Koivisto, J. Talvitie, K. Leppänen, and M. Valkama, "Beam-based device positioning in mmWave 5G systems under orientation uncertainties," in *2018 52nd Asilomar Conference on Signals, Systems, and Computers*, Oct 2018, pp. 3–7.

[26] Huawei. The world's largest automated container port operates using first-of-its-kind 5.8 GHz LTE. Accessed: Oct 15, 2020). [Online]. Available: https://e.huawei.com/topic/leading-new-ict-en/yangshan-port-case.html

[27] Ericsson. Ericsson and China Unicom announce 5G smart harbor at the Port of Qingdao. Accessed Oct 15, 2020). [Online]. Available: https://www.ericsson.com/en/press-releases/2019/2/ericsson-and-china-unicom-announce-5g-smart-harbor-at-the-port-of-qingdao

[28] Nokia, "5G smart sea port: Hamburg port authority," 2019, accessed on Oct 15, 2020. [Online]. Available: https://pf.content.nokia.com/t004f5-private-wireless-ports/use-case-5G-smart-sea-port

[29] R. M. Vaghefi and R. M. Buehrer, "Joint TOA-based sensor synchronization and localization using semidefinite programming," in *2014 IEEE International Conference on Communications (ICC)*, Jun. 2014, pp. 520–525, iSSN: 1938-1883.

[30] S. Fischer, "Observed time difference of arrival (OTDOA) positioning in 3GPP LTE," 2014, accessed on Oct 15, 2020. [Online]. Available: http://www.qualcomm.com/media/documents/files/otdoa-positioning-in-3gpp-lte.pdf

[31] E. Rastorgueva-Foi, M. Costa, M. Koivisto, K. Leppänen, and M. Valkama, "User positioning in mmW 5G networks using beam-RSRP measurements and kalman filtering," *FUSION Conference*, pp. 1–7, 06 2018.

[32] J. Hartikainen, A. Solin, and S. Särkkä, *Optimal Filtering with Kalman Filters and Smoothers – a Manual for the Matlab toolbox EKF/UKF*. Department of Biomedical Engineering and Computational Science, Aalto University School of Science, 2011.

[33] S. Kay, *Fundamentals of Statistical Signal Processing: Estimation Theory*. Prentice-Hall Signal Processing Series, 1993.

[34] METIS, "D1.4 Channel models," Feb. 2015. [Online]. Available: https://www.metis2020.com/wp-content/uploads/deliverables/METIS_D1.4_v1.0.pdf

[35] Port Technology, "Port of rotterdam hosts 5G innovation," 2018, accessed on Oct 15, 2020. [Online]. Available: http://www.porttechnology.org/news/port_of_rotterdam_hosts_5g_innovation/

[36] ——, "Port of hamburg becomes a 5G testing ground," 2018, accessed on Oct 15, 2020. [Online]. Available: http://www.porttechnology.org/news/port_of_hamburg_becomes_5g_testing_ground/

[37] ——, "Chinese ports see the fruits of5G," 2019, accessed on Oct 15, 2020. [Online]. Available: http://www.porttechnology.org/news/chinese-ports-see-the-fruits-of-5g/

[38] ——, "PSA begins smart port transformation," 2019, accessed on Oct 15, 2020. [Online]. Available: http://www.porttechnology.org/news/psa_begins_smart_port_transformation/

[39] H. Carlo, I. Vis, and K. Roodbergen, "Transport operations in container terminals: Literature overview, trends, research directions and classification scheme," *European Journal of Operational Research*, vol. 236, no. 1, pp. 1–13, 2014.

[40] M. B. Duinkerken and G. Lodewijks, "Routing of AGVs on automated container terminals," in *2015 IEEE 19th International Conference on Computer Supported Cooperative Work in Design (CSCWD)*, 2015, pp. 401–406.

[41] D. Overbeek, "Combining fixed-path and free- range AGV routing on a container terminal," Master's thesis, Delft University of Technology, Jun. 2017.

[42] B. Liang and Z. J. Haas, "Predictive distance-based mobility management for PCS networks," in *The Future is Now*, vol. 3. IEEE, 1999, pp. 1377–1384.

[43] T. Camp, J. Boleng, and V. Davies, "A survey of mobility models for ad hoc network research," *Wireless communications and mobile computing*, vol. 2, no. 5, pp. 483–502, 2002.

[44] F. Bai and A. Helmy, "A survey of mobility models," *Wireless Adhoc Networks. University of Southern California, USA*, vol. 206, p. 147, 2004.
[45] C. Bettstetter, "Smooth is better than sharp: a random mobility model for simulation of wireless networks," in *Proceedings of the 4th ACM international workshop on Modeling, analysis and simulation of wireless and mobile systems*. ACM, 2001, pp. 19–27.
[46] G. Sanfilippo, O. Galinina, S. Andreev, S. Pizzi, and G. Araniti, "A concise review of 5G new radio capabilities for directional access at mmwave frequencies," in *Internet of Things, Smart Spaces, and Next Generation Networks and Systems*. Springer, 2018, pp. 340–354.
[47] R. Pöhlmann, S. Zhang, T. Jost, and A. Dammann, "Power-based direction-of-arrival estimation using a single multi-mode antenna," in *14th Workshop on Positioning, Navigation and Communications (WPNC)*, 2017, pp. 1–6.
[48] J. Proakis and M. Salehi, *Digital Communications*, 5th ed. McGraw-Hill, 2008.
[49] G. Golub and V. Pereyra, "Separable nonlinear least squares: the variable projection method and its applications," *Inverse Problems*, vol. 19, no. 2, p. R1, 2003.
[50] B. Ottersten, M. Viberg, and T. Kailath, "Analysis of subspace fitting and ML techniques for parameter estimation from sensor array data," *IEEE Trans. Signal Proc.*, vol. 40, no. 3, pp. 590–600, Mar 1992.
[51] R. Behrens and L. Scharf, "Signal processing applications of oblique projection operators," *IEEE Trans. Signal Proc.*, vol. 42, no. 6, pp. 1413–1424, Jun 1994.
[52] P. Stoica and A. Nehorai, "MUSIC, Maximum Likelihood, and Cramér-Rao bound: further results and comparisons," *IEEE Trans. Acoust., Speech, and Signal Proc.*, vol. 38, no. 12, pp. 2140–2150, Dec 1990.
[53] M. Viberg, B. Ottersten, and T. Kailath, "Detection and estimation in sensor arrays using weighted subspace fitting," *IEEE Trans. Signal Proc.*, vol. 39, no. 11, pp. 2436–2449, Nov 1991.

Elizaveta Rastorgueva-Foi received M.Sc. in electrical engineering from Tampere University (TAU), Finland, in 2019, where she is currently working towards Ph.D. degree. Her research interests include statistical signal processing, positioning and location-aware communications in mobile networks with an emphasis on 5G and beyond.

Olga Galinina received her B.Sc. and M.Sc. degrees from the Department of Applied Mathematics, St. Petersburg State Polytechnical University of Peter the First, Russia and the Ph.D. degree from Tampere University of Technology (TUT) in 2015. Currently, she is a Finnish Academy Postdoctoral Researcher at Tampere University (TAU), Finland. Her research interests include applied mathematical modeling and analysis of wireless networks.

Mário Costa received the M.Sc. degree (Hons.) in communications engineering from the Universidade do Minho, Portugal, in 2008, and the D.Sc. (Tech.) degree in electrical engineering from Aalto University, Finland, in 2013. In 2014, he was a visiting post-doctoral research associate at Princeton University. Since 2014, he has been with Huawei Technologies Oy (Finland) Co., Ltd., as a senior researcher. His research interests include statistical signal processing and wireless communications.

Mike Koivisto received the M.Sc. degree in mathematics from Tampere University of Technology (TUT), Finland, in 2015, where he is currently pursuing the Ph.D. degree. From 2013 to 2016, he was a research assistant with TUT. He is currently a researcher at Tampere University (TAU), Finland. His research interests include positioning, with an emphasis on network-based positioning and the utilization of location information in future mobile networks.

Jukka Talvitie received the M.Sc. and D.Sc. degrees from Tampere University of Technology, Finland, in 2008 and 2016, respectively. He is currently a University Lecturer in the Faculty of Information Technology and Communication Sciences, Tampere University (TAU), Finland. His research interests include signal processing for wireless communications, radio-based positioning, radio link waveform design, and radio system design, particularly concerning 5G and beyond mobile technologies.

Sergey Andreev is an associate professor of communications engineering and Academy Research Fellow at Tampere University (TAU), Finland. He has been a Visiting Senior Research Fellow with King's College London, UK (2018-20) and a Visiting Postdoc with University of California, Los Angeles, US (2016-17). He (co-)authored more than 200 published research works on intelligent IoT, mobile communications, and heterogeneous networking.

Mikko Valkama received the D.Sc. (Tech.) degree (with honors) in electrical engineering from Tampere University of Technology (TUT), Finland, in 2001. In 2003, he was a visiting post-doc research fellow with SDSU, San Diego, CA. Currently, he is a Full Professor and Department Head of Electrical Engineering at the newly formed Tampere University (TAU), Finland. His research interests include radio communications, radio localization, and radio-based sensing, with particular emphasis on 5G and beyond mobile radio networks.